Environmental Science and Pollution Research (2024) 31:46484–46497
https://doi.org/10.1007/s11356-023-26043-z

SMART NANOMATERIALS FOR HEALTHCARE AND ENVIRONMENTAL APPLICATIONS: PERSPECTIVES IN NANOTOXICOLOGY

Construction of functionalized carbon nanotube@metal oxide nanocomposite for high-performance electrochemical measurement of antipyretic drug in water samples

Subramaniyan Vinoth[1] · **Sea-Fue Wang**[1]

Received: 21 November 2022 / Accepted: 16 February 2023 / Published online: 4 March 2023

Abstract

Acetaminophen (AP) acts as supportive clinical therapy for fever and dysmenorrhea. An overdose of AP may result in severe adverse diseases, such as liver dysfunction. In addition, AP is a key-listed environmental pollutant, which is difficult to degrade in the environment and has serious effects on living bodies. Therefore, the simple and quantitative determination of AP is highly relevant today. In this work, tin dioxide (SnO_2) nanoparticles with functionalized multi-walled carbon nanotube (*f*-MWCNT) as a hybrid composite were prepared by hydrothermal-assisted synthesis. The composite material was characterized by various spectral, morphological, and electrochemical tests. Electrochemical investigations were conducted using a SnO_2@*f*-MWCNT-reinforced electrode for the detection of AP. The composite electrode exhibited better functional properties, which facilitated electron transfer and enhanced electrical conductivity. The calculated low detection limit (LOD) of 0.36 nM is with a wide linear range of concentration from 0.001 to 673 µM. Additionally, the SnO_2@*f*-MWCNT-modified electrode exhibited good anti-interference capability, repeatability, reproducibility, storage, and operational stability. The developed SnO_2@*f*-MWCNT-modified electrode was applied to practical analysis in diverse water matrices (river, drinking, and pond) with acceptable recovery percentages. A synthesized nanoscale metal oxide electrocatalyst is of great interest and an active research area that serves as a foundation for the development of new, cost-effective electrochemical antibiotic drug sensors.

Keywords Electrochemical sensors · Acetaminophen · SnO_2 · *f*-MWCNT · Water pollutant detection · Hydrothermal-assisted synthesis

Introduction

Acetaminophen (AP-paracetamol: N-acetyl-para-aminophenol) has received wide recognition as an effective analgesic and antipyretic medicine (Wang et al. 2019). The AP is often prescribed to treat strep throat in addition to treating fever, headaches, joint pain, neuralgia, and dysmenorrhea (Chokkareddy et al. 2019). The AP drug has tremendous potential for regulating body temperature by selectively inhibiting the synthesis of prostaglandins in hypothalamic thermoregulatory centers while raising the pain threshold (Wei et al. 2021, Zhang et al. 2019). If the exposure of AP to humans exceeds the lethal dosage limit, it induces severe side effects like nausea, vomiting, and some serious harm to the liver (Lu et al. 2012). These effects are not only on humans, but also on the environment. Due to its non-prescriptive access, concentration of AP in domestic and medical wastes is high, and its contamination in surface waters has become an emerging water contaminant problem globally. Besides, increasing the concentration levels of AP (phenolic compounds) in water directly affects the sustainability of aquatic ecosystems while in portable water systems. As an emerging chemical pollutant, it poses a threat to the natural water bodies (Montaseri &Forbes

Responsible Editor: George Z. Kyzas

✉ Sea-Fue Wang
sfwang@ntut.edu.tw

[1] Department of Materials and Mineral Resources Engineering, National Taipei University of Technology, No. 1, Sec. 3, Chung-Hsiao East Rd, Taipei 106, Taiwan

2018). Therefore, monitoring the AP is important for both health care and environmental protection. The development of highly reliable and accurate methods to detect the AP is of prime important amongst researchers. Some of the traditional methods to detect AP are capillary electrophoresis (Zhang et al. 2000), high-performance liquid chromatography (HPLC) (Vanova et al. 2022), titration (Nabatian et al. 2022), spectrophotometry (Hadef et al. 2022), fluorescence (Keerthana et al. 2022), and electrochemistry (Arul et al. 2021a). In those, electrochemical detection requires less equipment and is also easy to operate than other methods (Balaji et al. 2022, Pourmadadi et al. 2022b). Electrochemical AP sensors have made great strides due to the development of nanotechnology. There have been many successful designs of electrochemical AP sensors incorporating metal oxides, carbon-based materials, semiconducting materials, and metal-organic framework (MOF) materials (Adhikari et al. 2016, Batool et al. 2021, Ma et al. 2019, Najeeb et al. 2022, Pourmadadi et al. 2022a, Yu et al. 2018). These materials are still being explored by researchers to develop AP sensors in environmental pollutants.

Among the many escalating environmental issues, the most serious of which is the lack of safe drinking water which poses a serious threat to human (Sharma et al. 2017). Because of their low cost, ease of synthesis, extremely porous character, and strong redox performance, carbon quantum dots and activated carbons from diverse natural feedstocks have been widely adopted for water purification (Bharathi et al. 2022, Gupta et al. 2022, Pourmadadi et al. 2023). Multi-walled carbon nanotubes (MWCNTs) possess an enormous potential to replace activated carbons in sensor technology in the near future. Babaei et al. synthesized nickel hydroxide nanoparticles/multi-walled carbon nanotubes composite electrode towards AP sensor to achieve the wide linear range 1–960 µmol/L and detection limit 0.25 µmol/L (Babaei et al. 2013). Due to the availability of a high number of active reactive sites, the open structure of carbon nanotubes (CNTs) has been widely preferred in numerous applications. The CNTs are proven to have high mechanical strength, considerable electrical characteristics, good field emission properties, and high thermal conductivity. The CNTs can be used as a reinforcing material to influence and enhance the mechanical property of composites and helps to develop smart materials/devices with outstanding Young's modulus (1 TPa), tensile strength (60 GPa), electrical conductivity (4105 S/m), and thermal conductivity (43000 W/mK) (Nadafan &Tohidifar 2020). Furthermore, adding surface functionalities like -OH, -COOH, and hybridization with different metal oxide nanoparticles such as Fe_2O_3, ZrO_2, SnO_2 CeO_2, MnO_2, polymers, biomolecules, etc. can significantly increase the catalytic properties (Rizwan et al. 2022, Sivasankarapillai et al. 2020). Metal oxide nanoparticles have been frequently employed to improve the characteristics of carbon nanotubes. Tin oxide (SnO_2) nanoparticles have recently been recognized as an important n-type semiconducting material with a broad band gap of 3.6 eV, generating a lot of research attention (Sharma et al. 2018). Tin oxide nanoparticles are often used in microelectronics, photo electronics, solar cells, biosensors, gas sensing, supercapacitors, field emission studies, and lithium-ion batteries due to their high electrical conductivity, photo-electronic property, low discharge voltage, high theoretical capacitance, and high sensitivity (Tamilalagan et al. 2020). In this work, we prepared SnO_2 nanoparticles anchored with *f*-MWCNT nanocomposite. It exhibits superior electrocatalytic traits of AP with modified glassy carbon electrode (GCE) due to an enhanced electrical conductivity and large specific surface area. This material has remarkable effectiveness, fast electron transfer rate, good stability, and interference resistance. Compared with previous literatures, the sensor displayed a low detection limit. In addition, the SnO_2@*f*-MWCNT/GCE has been successfully used to determine the presence of AP in environmental samples.

Experimental section

A brief description of the chemicals, materials, reagents, and instruments was included in the Supplementary Materials.

Synthesis of *f*-MWCNT

The functionalized MWCNT was produced utilizing a previously described method (Joseph et al. 2021). The pure MWCNT was weighed and distributed in a 1:1 ratio of HNO_3 and H_2SO_4 mixed solution. The liquid was then stirred for 30 min at 60 ℃ using a continuous magnetic stirrer. The solution combination was then subjected to ultrasonication for about 5 h. The well-distributed solution was then aged at room temperature. Finally, the black residue was centrifuged and allowed to cool to ambient temperature. The final residue obtained is known as *f*-MWCNT.

Synthesis of SnO_2-nanoparticles

The hydrothermal technique was used to prepare SnO_2 nanoparticles (Madhu et al. 2018). For 15 min, 0.2 M of $SnCl_4$. $5H_2O$ was dissolved in 30 mL of deionized water while stirring. After vigorous stirring, 0.1 M NaOH was added drop by drop to the above-mentioned reaction mixture. After agitating the resultant solution at ambient temperature for 30 min, the suspension mixture was transferred to an autoclave at 180 °C for 24 h before being centrifuged and washed with ultrapure water and ethanol several times to remove unreacted molecules. For 3 h, the product was dried in oven at 450 °C.

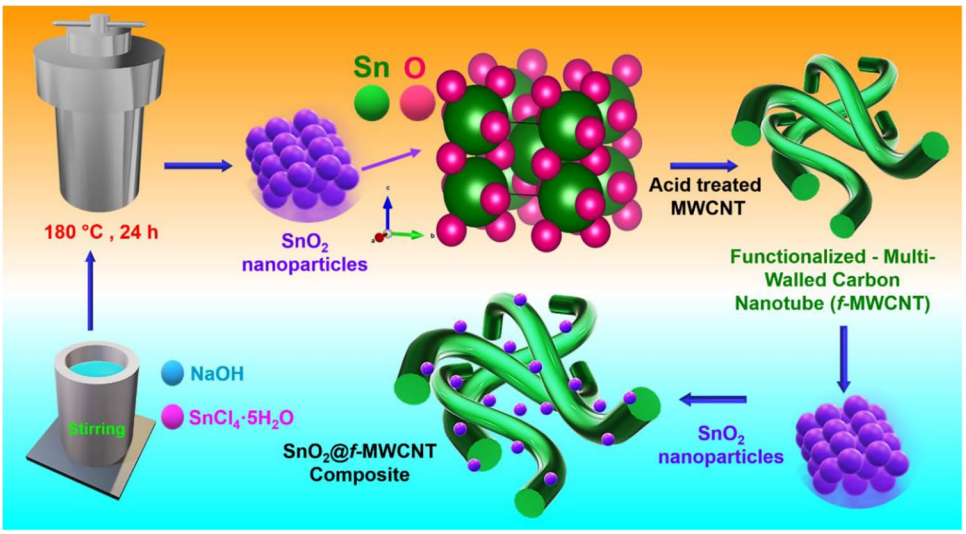

Scheme 1 Schematic representation of SnO_2 and SnO_2@*f*-MWCNT nanocomposite

SnO_2 nanoparticles were given to the resulting powder catalyst (Scheme 1).

Synthesis of SnO_2@*f*-MWCNT

The ultrasonication approach was used to synthesize the composite SnO_2@*f*-MWCNT. SnO_2 and *f*-MWCNT were combined in a 1:2 ratio to keep on sonication for 1 h at room temperature (Sriram et al. 2021). Then, the combined solution was rinsed with DI-H_2O and dried overnight in a drying oven set to 60 °C after, and the product was SnO_2@*f*-MWCNT composite (Scheme 1).

Fabrication of SnO_2@*f*-MWCNT electrocatalyst

The GCE was modified using SnO_2@*f*-MWCNT as a working electrode and used electrochemical sensor towards AP. Before using the working electrode, polishing with alumina powder removes unwanted contaminants. The resultant materials, *f*-MWCNT, SnO_2, and SnO_2@*f*-MWCNT, are drop casted on GCE surface in a 6-µL solution. The drop casting solutions were prepared by sonication for 20 min. The various customized electrodes are dried at 70 °C in a standard oven (Vinoth et al. 2022).

Electrochemical assay

The voltammetry analysis of AP was tested using modified composite electrodes surface. The relative standard deviation (RSD) was calculated using the following Eq. (1) (Arul et al. 2021b):

$$RSD = 100 \times \frac{SD}{(Mean\ of\ deviation)} \quad (1)$$

Result and discussion

Spectroscopic studies

The SnO_2@*f*-MWCNT was characterized by using X-ray diffraction (XRD) study to check the crystalline phase of the material as represented in Fig. 1A. The XRD pattern obtained for SnO_2 matched well with standard (Tetragonal (Cassiterite)—JCPDS Card # 00-005-0467) and revealed a space group number of 136 and (P_{42}/mnm) space group with confirmed lattice parameter (*a b*=4.7380 Å, *c* =3.1880 Å). The characteristic peaks in the obtained spectra are 26.5° (110), 33.8° (101), 37.95° (200), 38.9° (111), 42.6° (210), 51.7° (211), 54.7° (220), 57.8° (002), 61.8° (310), 64.7° (112), and 65.9° (301) which matches well with the literature (Wan et al. 2016). Notably, the composite form with *f*-MWCNT has a low peak which corresponds 25.8° (002) and 43.3° (100) to an inestimable connection of high intense, sharp peak of SnO_2 nanoparticles. The XRD was confirmed as synthesized SnO_2, *f*-MWCNT, and SnO_2@*f*-MWCNT. Besides, the average crystallite size was determined by Debye-Scherrer's equation using the prominent diffraction peak of the plane as follows Eq. (2):

$$D = (k\lambda \,/\, \beta \cos\,\theta) \quad (2)$$

Where *D*-average crystallite size (nm), *k*-Scherrer's constant (shape factor = 0.9), λ-X-ray wavelength (1.54 Å), β-FWHM (full width at half maximum) of the diffraction peak, and θ are Bragg's angle. The calculated average crystallite size was estimated to be 24 nm from all XRD peaks. Along with the ball-stick model, these SnO_2 have been reported in the form of tetragonal metal oxides (VESTA software) as shown in Fig. 1B.

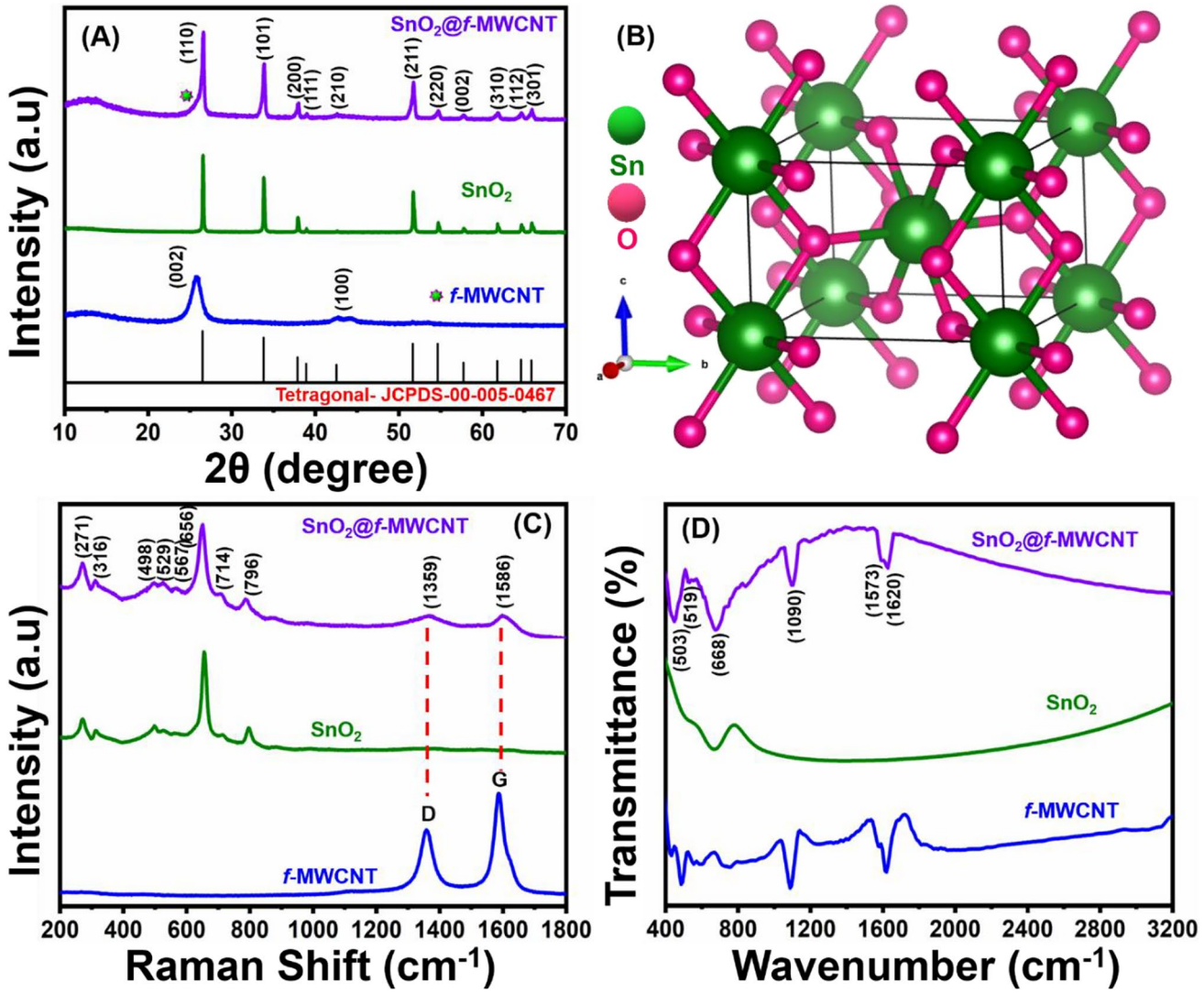

Fig. 1 **A** XRD patterns of SnO_2, *f*-MWCNT, and SnO_2@*f*-MWCNT nanocomposite, **B** Crystal structure of SnO_2-cassiterite (ball and stick model), **C** Raman spectrum, and **D** FTIR spectra of SnO_2, *f*-MWCNT, and SnO_2@*f*-MWCNT nanocomposite respectively

The room temperature of Raman spectrum of SnO_2, *f*-MWCNT, and SnO_2@*f*-MWCNT samples has taken between the wavelengths 200 and 1800 cm^{-1}. Generally, it is used to study the crystal structure of materials which can be observed due to interaction or overlapping. It is assigned at 271, 316, 498, 529, 567, 656, 714, and 796 cm^{-1} with vibrational modes of E_u, A_{1g}, E_g, A_{2g}, and B_{2g} respectively (Haddad et al. 2017). Besides, the *f*-MWCNT compared with finally modified composite (SnO_2@*f*-MWCNT) possesses binary bands of sp^3-hybridized disordered structure of D-band at 1359 cm^{-1} and also a sp^2-hybridized carbon of G-band at 1586 cm^{-1} respectively (Fig. 1C). The spectrum consists of peaks corresponding to both SnO_2@*f*-MWCNT composite. FTIR spectrum of prepared pure SnO_2 with *f*-MWCNT of the absorption bands are 503, 519, 668, 1090, 1573, and 1620 cm^{-1} (Fig. 1D). The observed peaks at 519 and 668 cm^{-1} represent Sn-O and O-Sn-O modes. Then, the other bands such as 503, 1090, 1573, and 1620 cm^{-1} are observed with acid-treated *f*-MWCNT. The relatively narrow peak at 1620 cm^{-1} corresponding to stretching vibration of C=O mode and C=C bonds will have the presence of assigned 1573 cm^{-1} aromatic peak, and other narrow peaks was observed at 1090 cm^{-1} C-O alkoxy group**.** Finally, we confirmed the formation of SnO_2@*f*-MWCNT composite by using sonication method. So, it will be more suitable for an electrocatalytic activity to enhance electron transfer properties.

XPS analysis

XPS analysis was used to investigate the chemical states and elemental composition of the synthesized

SnO_2@*f*-MWCNT nanocomposite. The survey spectrum of the SnO_2@*f*-MWCNT nanocomposite shows clear peaks of Sn, O, and C (Fig. 2A). In the XPS spectra of Sn 3d, three distinctive peaks of 485.8 and 494.2, 497.5 eV can be assigned to Sn $3d_{5/2}$ and Sn $3d_{3/2}$, indicating the presence of Sn^{4+} on the surface of carbon fiber. The spin–orbit splitting energy between Sn $3d_{5/2}$ and Sn $3d_{3/2}$ is 8.4 eV (Pallavolu et al. 2022). SnO_2 was initiated through the reaction of $Sn(OH)_4$ in alkaline solution at high temperatures and pressures (Fig. 2B). The O 1s spectra were separated into two components: 529.9 eV of O–C and 531.9 eV of O=C (Fig. 2C).

The C 1s region spectra were divided into three peaks, indicating the existence of carbon in three distinct chemical environments. Three peaks with energies of 283.6 eV, 284.5 eV, and 285.2 eV, respectively, corresponded to sp^2 hybridized C–C and sp^3 hybridized C=O bonds and C=O–C (Fig. 2D). Finally, we conformed SnO_2 nanoparticles decorated on nanotubes, for which observed in the spectrum analysis provides a clearly through valence bond formation.

Surface morphology

Analytical grade chemicals were employed in the production of SnO_2@*f*-MWCNT nanocomposites for analysis using FESEM and TEM (Fig. 3). Using FESEM, high resolution of the nanomaterials SnO_2, *f*-MWCNT, and SnO_2@*f*-MWCNT was captured in order to gain a thorough understanding of the surface morphology. It displays the final FESEM of the SnO_2 particles created in this work using the hydrothermal technique. The FESEM of the synthesized SnO_2 depicts an asymmetrical nanoparticle with a metal oxide size that was

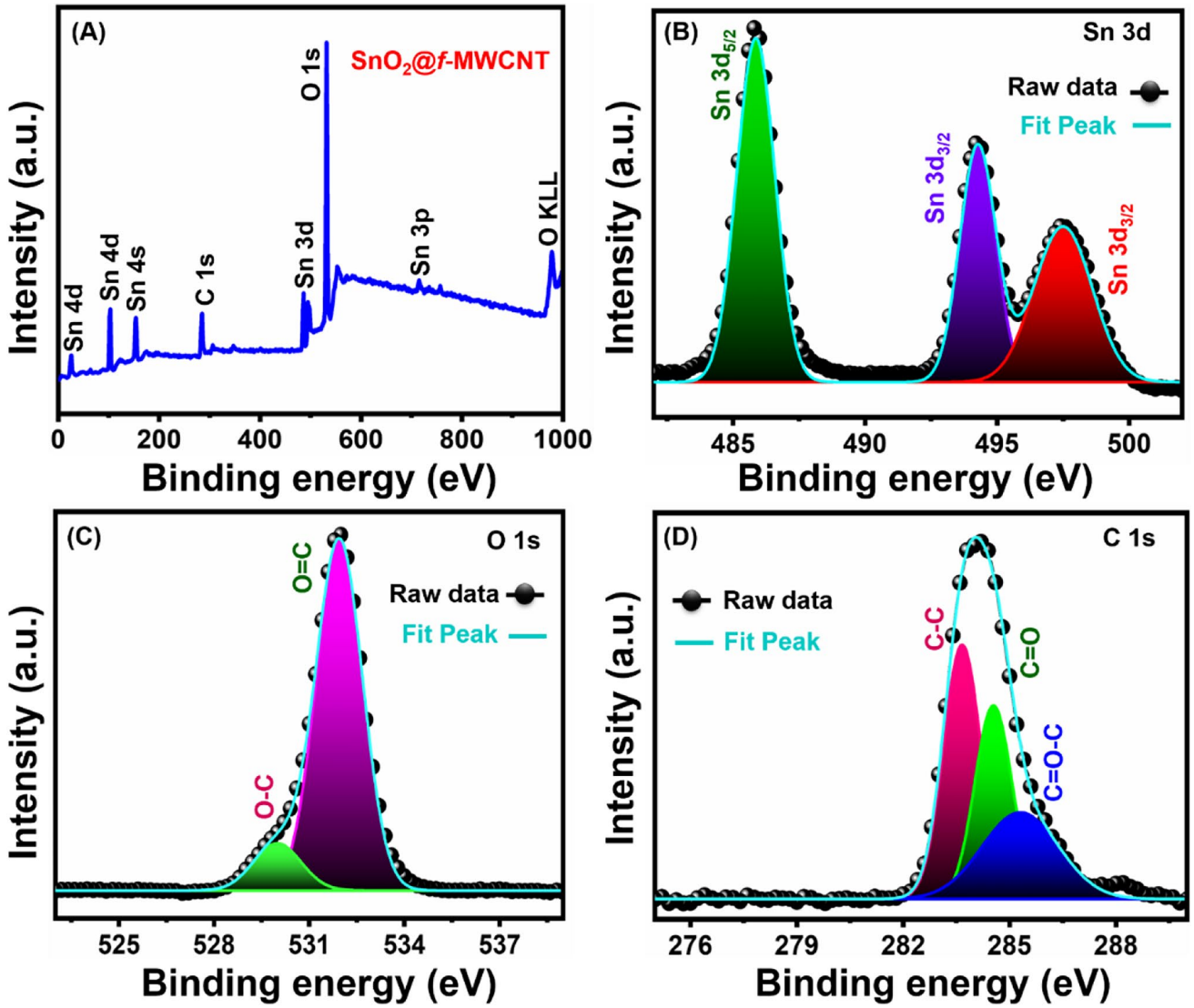

Fig. 2 XPS spectrum of overall spectra of SnO_2@*f*-MWCNT (**A**), Sn 3d (**B**), O 1s (**C**), and C 1s (**D**)

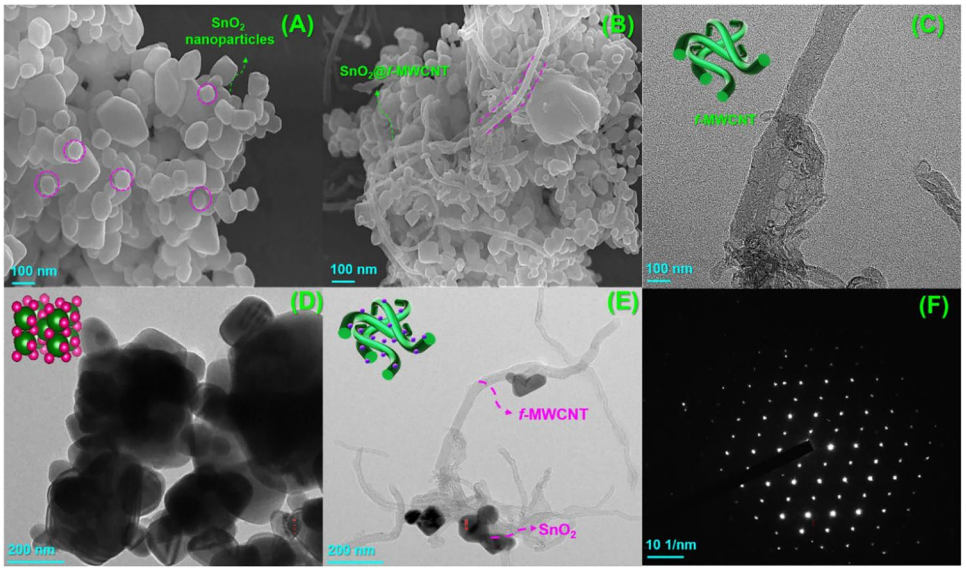

Fig. 3 FESEM image of **A** SnO_2 and **B** SnO_2@*f*-MWCNT. TEM image of **C** *f*-MWCNT, **D** SnO_2, **E** SnO_2@*f*-MWCNT nanocomposite, and **F** SAED pattern

determined to be around 100 nm in length (Fig. 3A). We also examined the resulting *f*-MWCNT material (Fig-S1(A)). In the FESEM, we can clearly see the *f*-MWCNT narrow tube-like structure (Fig. 3B). We also performed FESEM analysis SnO_2@*f*-MWCNT nanocomposites where both the material in the composite is clearly seen. The produced nanocomposite has also undergone elemental mapping, as shown in Fig-S1 (B-G). Tin (Sn), oxygen (O), and carbon (C) are respective elemental mappings. Thus, we were able to detect the surface morphology of synthesized materials by performing FESEM characterization and elemental mapping. SnO_2@*f*-MWCNT tube and particle network provides a wide accessible surface area for electrolyte penetration, starts quick electrochemical interactions with electrolyte ions, and improves their sensitivity and rate capability. The elemental analysis and energy dispersive X-ray (EDX) spectra of the SnO_2@*f*-MWCNT nanocomposite are shown (Fig-S1 (G) insert image). Several elements such as Sn, O, and C were detected in the manufactured sample without any contaminants based on the EDX spectrum. Furthermore, the SnO_2@*f*-MWCNT material homogenous distributed and coexisted in Sn, O, and C elements. And also, we measured the particle size distribution of SnO_2 nanoparticles (Fig-S2).

To fully comprehend the nanostructures of the SnO_2@*f*-MWCNT composite, TEM examinations were conducted. It displays a TEM image of *f*-MWCNT narrow tube-like structure and demonstrates that it is possible to find material that can change morphology into nanotubes (Fig. 3C). SnO_2 nanoparticles demonstrate that the particles are naturally spherical (Fig. 3D). In the SnO_2 nanoparticles shown on the *f*-MWCNT nanotubes, a deep black area is emphasized. Both the SnO_2 and *f*-MWCNT components are connected to one another, and there are important interactions between the two materials (Fig. 3E). Additionally, the produced materials of pure SnO_2 are confirmed by the selective area electron diffraction pattern (SAED) in the numbers 110, 112, and 221 (Fig. 3F).

Electrochemical impedance spectroscopy (EIS)

In order to verify the interfacial charge transfer electrons at the electrode surface, an analogous circuit can be fitted using impedance values. The electrochemical interfacial charge transfer properties of GCE and modified electrode surfaces were measured in a working solution containing redox pairs of 5 mM $[Fe(CN)_6]^{3-/4-}$ and 0.1 M KCl (Fig. 4A). At high frequencies, the unmodified electrode surface appears to have a large semicircle section. Despite the lowered charge transfer rate and mass at the surface of the redesigned electrode, the results demonstrate a high charge transfer resistance (R_{ct}). As a result of high frequencies, semicircle of the modified SnO_2@*f*-CNT/GCE (88.2 Ω) was smaller than that of alone GCE (197.7 Ω), *f*-CNT/GCE (171.8 Ω), and SnO_2/GCE (97.2 Ω), respectively. In fact, the aforementioned modified surfaces have actually increased electron kinetics rates, which reduces the mass transfer resistance. This higher conductivity of the modified electrode (SnO_2@*f*-CNT) results in a noticeable increase in electron charge transfer, and it was calculated from the following (Eq. (3)) (Vinoth &Wang 2022b):

$$R_{ct} = \frac{RT}{(n^2F^2K_sC)} \tag{3}$$

R is the gas constant (8.314 J mol^{-1} K^{-1}), T is the temperature (330 K), n is the number of electrons, K_s is the rate constant, C is the concentration of the redox probe, R_{ct} is

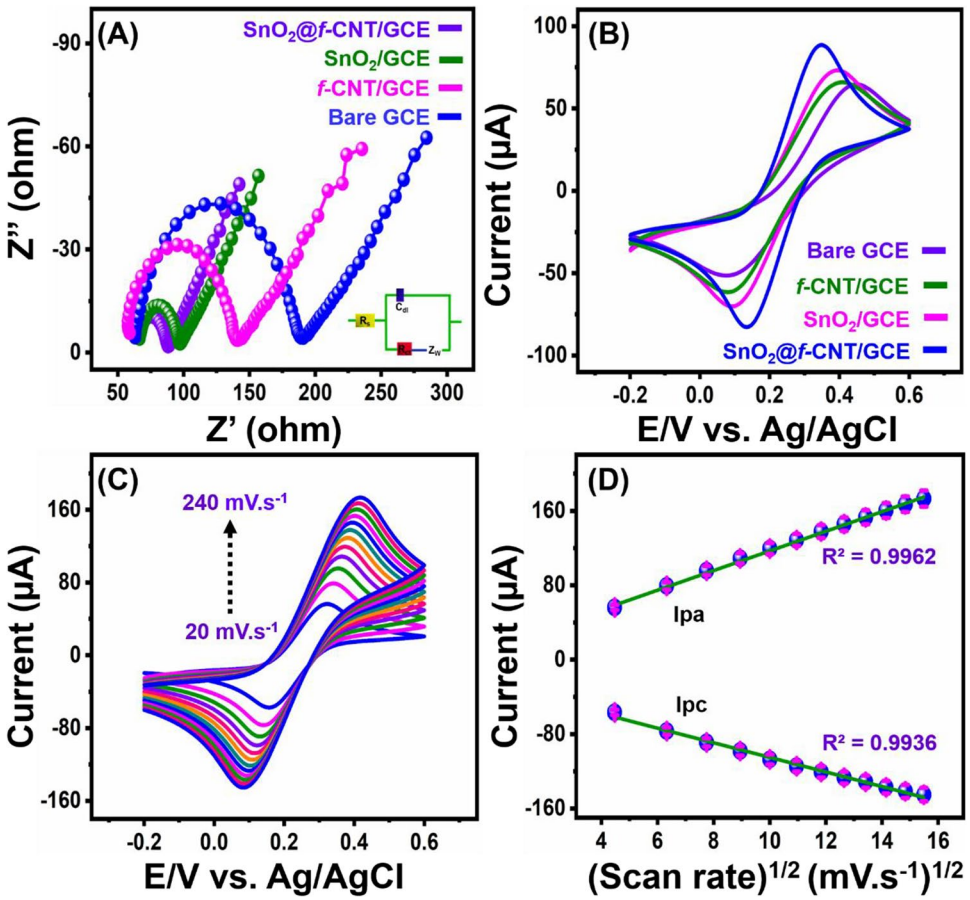

Fig. 4 **A** EIS. **B** CVs of control and modified electrodes in redox probe of $Fe(CN)_6^{3-/4-}$. **C** Effect of scan rate from 20 to 240 mV.s^{-1}, with corresponding square root of calibration plots (**D**)

the charge transfer resistance, and F is the Faraday constant (96485.33 s A/mol). Another interesting parameter for electrochemical sensors is the electroactive surface area. Modified electrode surfaces were used to monitor the surface area by voltammetry response under reversible active redox probe of $[Fe(CN)_6]^{3-/4-}$. Figure 4B shows the CVs for redox probe of ferric and ferro system at SnO_2@f-CNT/GCE, f-CNT/GCE, SnO_2/GCE, and bare GCE under the potential scan between −0.2 and 0.6 V. The redox behavior of surfaces for bare GCE, f-CNT/GCE, SnO_2/GCE, and SnO_2-bounded f-CNT is of I_{pa} = 64.6, 66.4, 73.1, and 88.2 µA, respectively. The large active surface area of composite electrode showed facile synergistic effect between individual functions of SnO_2 and f-CNTs. Furthermore, in efficient adsorption of SnO_2 on f-CNT, the composite could potentially affect the anodic and cathodic current intensity, and it was proving the facility of electron transfers. In order to calculate the rate reaction of modified electrodes, the Randles-Sevcik equation (Eq. (4)) was used (Vinoth &Wang 2022a).

$$I_P = 2.69 \times 10^5 \times ACn^{3/2}D^{1/2}v^{1/2} \quad (4)$$

Where D is the diffusion coefficient (7.60×10^{-6} cm^2 s^{-1}), n is the number of transferred electrons (n = 1), A is the surface area of the electrode (cm^2), I_p is the slope of peak current (A), ν is the scan rate (V.s^{-1}), and C is the concentration of a solution (µmol cm^{-3}). The higher surface area of SnO_2@f-CNT (0.256 cm^2) is highly depended on the surface defect than control electrodes. In order to verify the kinetic behavior of modified electrodes, the effect of scan rate was investigated from 20 to 240 mV.s^{-1} (Fig. 4C). Based on the linear plots (R^2 = 0.9962 (I_{pa})) (R^2 = 0.9936 (I_{pc})) and peak-to-peak separation values, the system has diffusion-controlled process (Fig. 4D).

Effect of modified electrode

Cross-checking the electrochemical activity of modified electrodes requires a catalytic investigation of AP. Figure 5A shows the CV signals for oxidation of AP at modified electrodes under the potential scan between −0.2 and 0.8 V in pH-7.0 as an electrolyte. The signal response of bare GCE (I_{pa} = +4.219 µA) was observed, but current behavior was significantly affecting at higher detection potential of +0.55 V. Additionally, f-CNT/GCE (I_{pa} = +5.58 µA) and SnO_2/GCE (I_{pa} = +8.23 µA) had significantly higher peak current of AP than control bare GCE. Interestingly, SnO_2@f-CNT/GCE had enhanced current

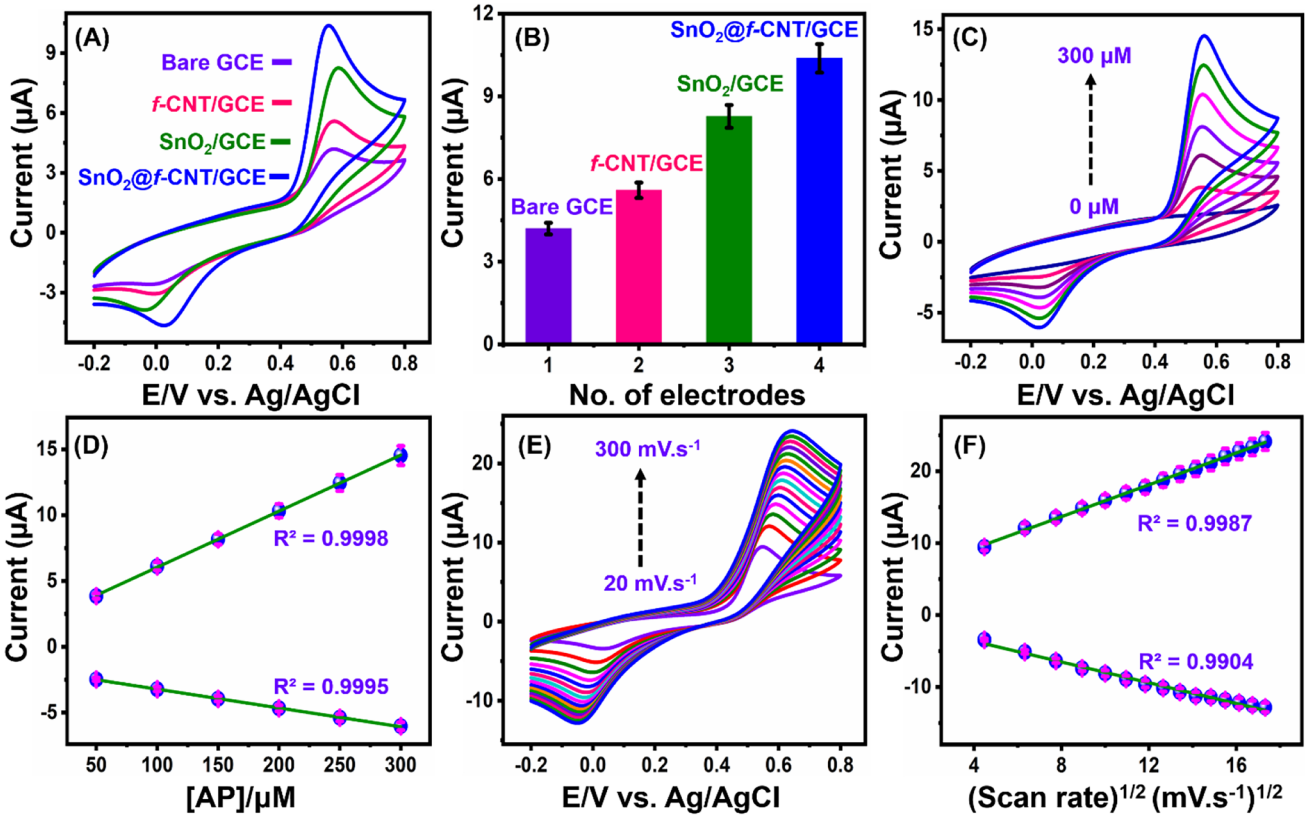

Fig. 5 **A** CVs for AP (200 μM) at bare GCE, *f*-CNT/GCE, SnO_2/GCE, and SnO_2@*f*-CNT/GCE, with corresponding bar diagram (**B**). **C** CVs for different concentration of AP. **D** Calibration plots of current vs concentration. **E** Effect of scan rate from 20 to 300 $mV.s^{-1}$. **F** The linearity plots of scan rate

signal (I_{pa} = +10.4 μA) and clear sharp peak potential (E_{pa} = +0.55 V) than other control electrodes.

Therefore, the significance of electrocatalytic performance on SnO_2@*f*-CNT/GCE identified the strong electron transfer towards AP. Figure 5B shows a bar diagram of current signal against and various modified electrodes of AP. As a result of the increased active surface area and improved electron transfer between SnO_2 and *f*-CNT, the composite electrode steadily increased the sensitivity efficiency of concentration from 0 to 300 μL (Fig. 5C). A calibration plot was drawn between the oxidation peak current and concentration of AP and linear regression coefficient values expressed as $I_{pa}(\mu A) = 0.042 \times +1.788$ ($R^2 = 0.9998$) and $I_{pc}(\mu A) = -0.014 \times -1.787$ ($R^2 = 0.9995$) (Fig. 5D). Based on the results of linear plot, SnO_2@*f*-CNT/GCE has revealed the first-order kinetics of AP. The effect of scan rate for 200 μM of AP at SnO_2@*f*-CNT/GCE is shown in Fig. 5E. The linear changes of oxidation peaks while tuning the scan rate from 20 to 300 $mV.s^{-1}$ and linear plot of square of the scan root suggested ($I_{pa}(\mu A) = 1.107 \times +4.829$ ($R^2 = 0.9987$) and $I_{pc}(\mu A) = -0.722 \times -0.732$ ($R^2 = 0.9904$)) that detection system has adsorption-controlled process (Fig. 5F).

Effect of pH

Voltammetry technique was used to investigate the effect of pH on the electrocatalytic activity of modified SnO_2@*f*-CNT/GCE surface and target analyte (Fig. 6A). The redox current increases with increasing electrolytic pH medium until it reaches 7.0, and after that, current signal was minimized. The linear calibration plot of pH versus potential of AP oxidation is as follows: $I_{pa}(A) = 0.041x + 0.840$ with correlation coefficient of $R^2 = 0.9982$ are shown in Fig. 6B. The significant changes of peak potential for AP are as a result of protons participating in the electrochemical detection mechanism.

According to this study, stability was truthfully affected by while switching the electrolyte medium of both basic (11.0) and acidic pH (3.0), respectively. In pH environment below 3.0, there are many protons participating to form benzoquinone. Furthermore, the AP became unstable at pH levels above or equal to 9.0 due to an abundance of hydroxide ions. In spite of this, AP remained stable in pH ranges of 5.0 to 11.0; however, dimerization might be responsible for the inherent instability. pH 5.0 to 11.0 showed strong redox signals, with

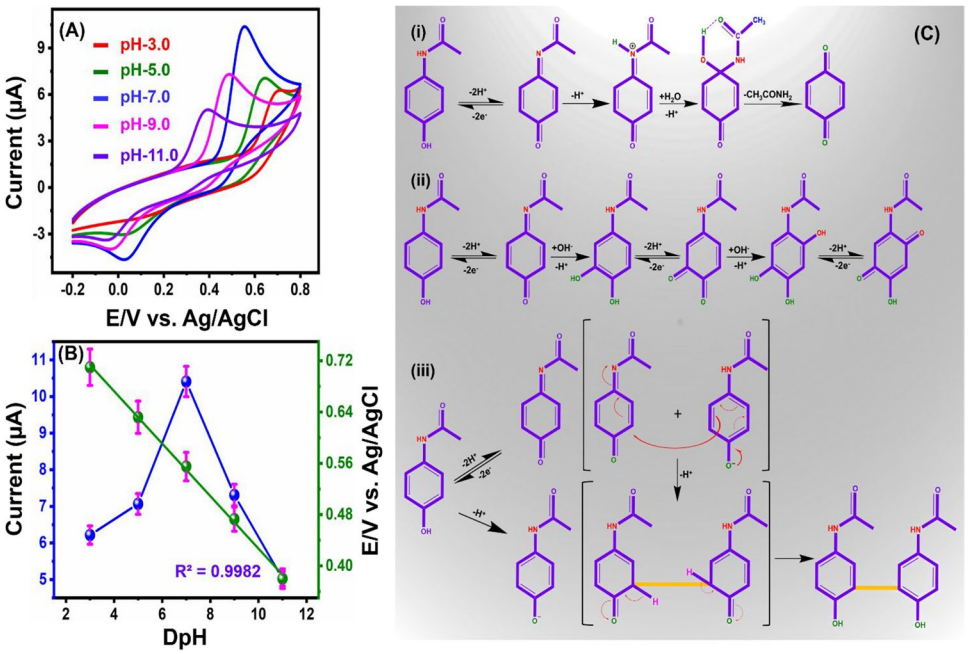

Fig. 6 **A** The optimized pH studies of AP. **B** The calibration plot of pH vs current with possible sensing mechanism (**C**)

the detection peak potential slightly changing towards a cathodic peak. The pH 7.0 electrolyte was found to be effective for sensing of AP (Fig. 6C). Based on the slope value, *m* and *n* were applied into the Nernst equation (Eq. (5)).

$$E_p = E^o - \left(\frac{0.0592m}{n}\right) pH \tag{5}$$

From the theoretical calculation, the m/n ratio was found to be 0.69 suggesting that the mechanical accepts of AP

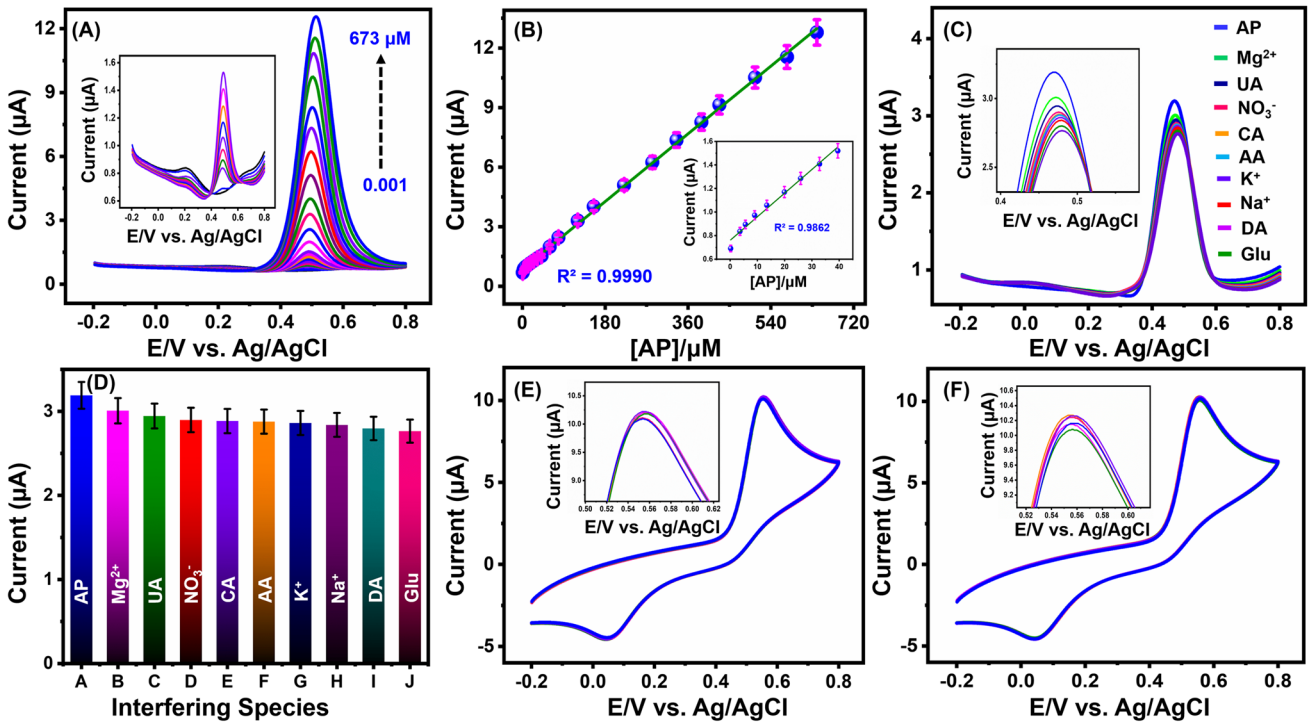

Fig. 7 **A** DPVs for linear concentration range of AP from 0.36 to 673 μM at SnO_2@*f*-CNT. **B** Linearity plot for current vs concentrations of AP. **C** Anti-interfering analysis of different species with corresponding bar chart diagram. **D** Bar chart diagram for effect interferences. **E** Reproducibility and **F** repeatability studies of modified electrodes

Table 1 Analytical parameters for the determination of AP at SnO_2@*f*-MWCNT-modified electrode with previous report

Electrode materials	Detection method	LOD (nM)	Linear range (μM)	Ref
[a]PS-PNIPAm-PS/MWCNTs-GQDs	[j]DPV	66	0.1–103.0	(Zhao et al. 2019)
[b]NiCu-CAT	DPV	5000	5–190	(Wang et al. 2020)
[c]AuPd/GN-CNTs-IL	DPV	50	0.1–10	(Yang et al. 2021)
[d]MOFs/ERGO	DPV	16	0.6–120	(Ma et al. 2019)
[e]CNT/SBA/Ag-PE	DPV	38	0.12–110	(Tkachenko et al. 2021)
[f]γ-Fe_2O_3/CNTs	DPV	46	2.5–385	(Cai et al. 2021)
[g]MIP/pABSA	DPV	43	0.05–100	(Teng et al. 2015)
[h]Pt/CeO_2@Cu_2O	[k]CV	50	0.4–32	(Rajamani & Peter 2018)
[i]Au-rgo/poly(L-cys)	CV	500	1–200	(Zhang et al. 2020)
Pyrolytic carbon films	DPV	1400	15–250	(Keeley et al. 2012)
Graphene ink film	DPV	2700	10–500	(Fu et al. 2018)
SnO_2@*f*-MWCNT	DPV	0.36	0.001-673	This work

[a]Poly(styrene-b-(N-isopropylacrylamide)-b-styrene)/multi-walled carbon nanotubes−graphene quantum dots
[b]Catecholate
[c]AuPd nanoparticles−ionic liquid (IL) functionalized graphene−carbon nanotube nanocomposite
[d]Metal organic frameworks/electroreduction graphene oxide
[e]Carbon nanotube/Santa Barbara Amorphous/silver nanoparticles
[f]γ-phase iron oxide/carbon nanotubes
[g]Molecular-imprinted polymer/poly (p-aminobenzene sulfonic acid)
[h]Platinum/cerium oxide@cuprous oxide
[i]Au-reduced graphene oxide/poly(L-cysteine)
[j]Differential pulse voltammetry
[k]Cyclic voltammetry

oxidation participated. In this case, m and n are the same numbers of protons and electrons, E_p is the peak potential, and E^o is the standard potential.

Electrochemical determination of AP

Differential pulse voltammetry (DPV) is a superior analytical method for sensitive detection of target by electrochemically. In Fig. 7A, DPV analysis was performed on SnO_2@*f*-CNT/GCE at a 50 $mV.s^{-1}$ with gradual concentration increment of AP from low to high level. There is a wide linear range concentration from 0.001 to 673 μM, and current signal was significantly enhanced with correlation coefficient $R^2 = 0.9862$ and 0.9990 illustrated in Fig. 7B. In order to determine AP, the oxidation peak current was absorbed toward the positive peak potential caused by the bare electrode surface. In addition, the enhanced oxidation peak currently seen during AP detection occurs as a result of electrons interacting with the composite electrode surface. Calculating the LOD of AP using the calibration plot and 3.3σ/slope formula yielded 0.36 nM and sensitivity of 0.262 μA μM^{-1} cm^{-2}. The present sensor report of SnO_2@*f*-CNT-modified GCE showed significant analytical performance than excited methods. Compared to the studies (Table 1), the SnO_2@*f*-CNT-modified electrode has a low LOD and wide linear operating range than the most previous literatures (Cai et al. 2021, Fu et al. 2018, Keeley et al. 2012, Ma et al. 2019, Rajamani &Peter 2018, Teng et al. 2015, Tkachenko et al. 2021, Wang et al. 2020, Yang et al. 2021, Zhang et al. 2020, Zhao et al. 2019) with detection of AP. Considering all of this suggests its promising potential for real sample analysis of AP from environmental samples.

Anti-interference and selectivity studies

The properties of anti-interference, stability, and reproducibility are highly important for electrochemical target sensors. Hence, the developed sensing system continues the investigation of selectivity, accuracy, and other special performances. Initially, the anti-interference behavior of SnO_2@*f*-CNT/GCE was investigated in AP with other possible interfering biological substances. In Figure 7C, DPV signal response for AP with possible interfering metal ions and biological chemical components includes (A) acetaminophen (AP), (B) magnesium (Mg^{2+}), (c) uric acid (UA), (D) nitrate (NO_3^-), (E) caffeic acid (CA), (F) ascorbic acid (AA), (G) potassium (K^+), (H) sodium (Na^+), (I) dopamine (DA), and (J) glucose (Glu). In order to verify the selectivity test, 20-fold higher concentration of above possible metal ions and biomolecules

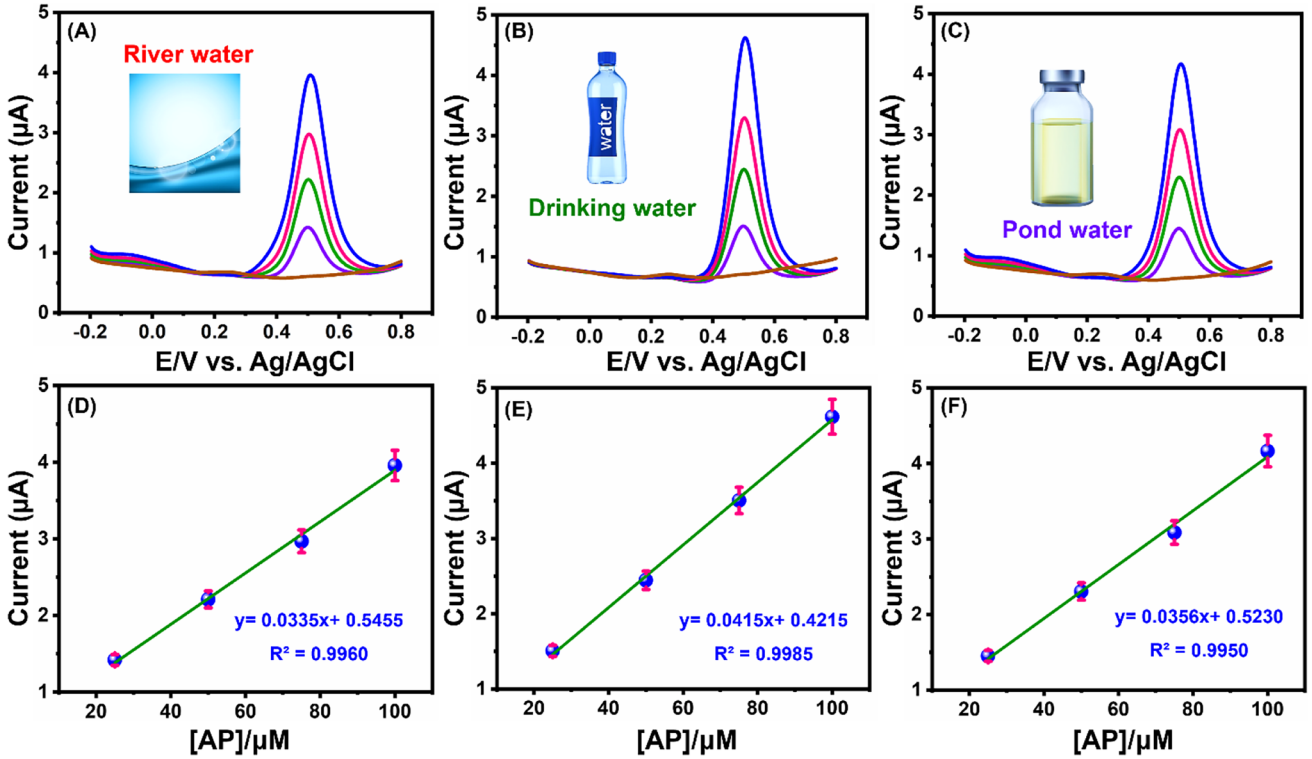

Fig. 8 **A**–**C** DPVs for practical utility results of AP in presence of various sources of water samples with corresponding linear plots (**D**–**F**)

is added with the same electrolytic media. Interestingly, no significant current changes were observed, and it may due to size exclusion effect, interfacility chemical charges, mobility of ions, and selective targeted active porosity of SnO_2. Figure 7D shows a bar graph chat of interfering species vs. current and relative error vs. interfering species (Fig-S3(A)). As a result, the obtained results were satisfactory in terms of anti-interference. The repeatability test was conducted with six different SnO_2@*f*-CNT-modified electrodes for catalytic response of AP (200 µM) with RSD of 3.46%, as shown in Fig. 7E. The repeatability of modified SnO_2@*f*-CNT in (200 µM) AP was continuously assessed by repeating the experiment six times. The repeatability of this experiment was good, with an RSD value of 2.41% (Fig. 7F). Furthermore, Fig-S3(B-C) shows a bar graph for reproducibility and repeatability. The oxidation current response of AP (200 µM) was investigated by 50 continuous potential cycles, and results show 5% of variant Fig-S3(D). The physicochemical characteristics and structural capability of the proposed SnO_2 with *f*-CNT delivered a high performance of catalytic activity including facile rate reaction and an extended active site.

Practicability analysis

AP has potentially addressed human health and aquatic environmental pollution and is highly relevant to quantitative analysis. In order to determine the quantitative amount of AP in various samples including ponds, rivers, and drinking waters. The detailed pre-treatment process of real samples was given in supporting information. To determine the concentration of AP in real samples, a modified electrode sensor made of SnO_2@*f*-CNT was evaluated by DPV. In electrolyte (pH 7.0), the present real-time monitoring sensor samples did not reveal a current response. Figure 8A–C shows the AP oxidation current signal at +0.55 V using the standard addition of AP. DPV response and calibration plot were drawn based on results of environmental samples as follows: I_{pa}(A) = 0.0335x + 0.5455, 0.0415x + 0.4215, and 0.0356x + 0.5230 with correlation coefficients of R^2 = 0.9960, 0.9985, and 0.9950 was found in drinking, pond, and river waters (Figure 8D–F), respectively. Following that, the oxidation current signal steadily increased in the same electrolytic medium, and attentively signal response of AP was strengthen without affecting the detection potential. These findings clearly demonstrate that the current sensor's viability will not positively affect the detection of AP in real samples.

Conclusions

In summary, a reliable electrochemical detection of AP was achieved by SnO_2 composite with *f*-CNT. The hydrothermal approach was used to synthesize the metal oxide nanomaterial,

and sonication technique was used to produce the composite SnO_2@*f*-CNT. The composite material was analyzed by spectral (XRD, Raman, and FTIR) morphological characterization (FE-SEM, TEM, EDX, and elemental mapping). The sensing system of AP delivered an extended linear wide range concentration, low detection limit, and high sensitivity than other existing similar nanocomposite-modified electrodes. SnO_2@*f*-CNT-modified electrode was successfully used to detect AP in environmental water samples and showed a good recovery percentage result. These superior catalytic activities of hybrid composites could be applied to point-of-care devices in real-time environmental samples to save human life at an earlier stage of infection.

Supplementary Information The online version contains supplementary material available at https://doi.org/10.1007/s11356-023-26043-z.

Author contribution Subramaniyan Vinoth: writing—original draft, data curation, methodology, formal analysis, conceptualization
Sea-Fue Wang: validation, formal analysis, resources, supervision, funding acquisition

Funding The authors thank the Ministry of Science and Technology (MOST-108-2221-E-027-063) and the National Taipei University of Technology (NTUT) for the financial encouragement to support this work.

Data availability Data will be made available upon the reasonable request.

Declarations

Ethical approval Not applicable.

Consent to participate Not applicable.

Consent for publication Not applicable.

Competing interests The authors declare no competing interests.

References

Adhikari B-R, Govindhan M, Schraft H, Chen (2016) Simultaneous and sensitive detection of acetaminophen and valacyclovir based on two dimensional graphene nanosheets. J. Electroanal. Chem 780:241–248. https://doi.org/10.1016/j.jelechem.2016.09.023

Arul P, Gowthaman N, Narayanamoorthi E, John SA, Huang S-T (2021) Synthesis of homogeneously distributed gold nanoparticles built-in metal free organic framework: electrochemical detection of riboflavin in pharmaceutical and human fluids samples. J Electroanal Chem 887:115143

Arul P, Huang S-T, Gowthaman N, Mani G, Jeromiyas N, Shankar S, John SA (2021) Electrocatalyst based on Ni-MOF intercalated with amino acid-functionalized graphene nanoplatelets for the determination of endocrine disruptor bisphenol A. Anal Chim Acta 1150:338228

Babaei A, Sohrabi M, Taheri AR (2013) Highly sensitive simultaneous determination of L-dopa and paracetamol using a glassy carbon electrode modified with a composite of nickel hydroxide nanoparticles/multi-walled carbon nanotubes. J. Electroanal. Chem 698:45–51. https://doi.org/10.1016/j.jelechem.2013.01.021

Balaji R, Maheshwaran S, Chen S-M, Tamilalagan E, Chandrasekar N, Ethiraj S, Samuel MS (2022) Fabricating BiOI nanostructures armed catalytic strips for selective electrochemical and SERS detection of pesticide in polluted water. Environ Pollut 296:118754

Batool M, Nazar MF, Awan A, Tahir MB, Rahdar A, Shalan AE, Lanceros-Méndez S, Zafar MN (2021) Bismuth-based heterojunction nanocomposites for photocatalysis and heavy metal detection applications. Nano-Struct Nano-Objects 27:100762

Bharathi D, Nandagopal JGT, Ranjithkumar R, Gupta PK, Djearamane S (2022) Microbial approaches for sustainable remediation of dye-contaminated wastewater: a review. Arch Microbiol 204:169. https://doi.org/10.1007/s00203-022-02767-3

Cai X-Q, Zhu K, Liu B-T, Zhang Q-Y, Luo Y-H, Zhang D-E (2021) γ-Fe2O3/CNTs composites for electrochemical detection of paracetamol: synthesis, phase transition and enhanced properties. J Electrochem Soc 168:057511

Chokkareddy R, Thondavada N, Bhajanthri NK, Redhi GG (2019) An amino functionalized magnetite nanoparticle and ionic liquid based electrochemical sensor for the detection of acetaminophen. Anal. Methods 11:6204–6212. https://doi.org/10.1039/C9AY01743G

Fu L, Xie K, Zheng Y, Zhang L, Su W (2018) Graphene ink film based electrochemical detector for paracetamol analysis. Electronics 7:15. https://doi.org/10.3390/electronics7020015

Gupta M, Savla N, Pandit C, Pandit S, Gupta PK, Pant M, Khilari S, Kumar Y, Agarwal D, Nair RR (2022) Use of biomass-derived biochar in wastewater treatment and power production: a promising solution for a sustainable environment. Sci. Total Environ 153892. https://doi.org/10.1016/j.scitotenv.2022.153892

Haddad N, Ben Ayadi Z, Mahdhi H, Djessas K (2017) Influence of fluorine doping on the microstructure, optical and electrical properties of SnO 2 nanoparticles. J Mater Sci: Mater Electron 28:15457–15465. https://doi.org/10.1007/s10854-017-7433-1

Hadef Y, Nekkaa A, Titel F, Dalia F (2022) Cost-effective and earth-friendly chemometrics-assisted spectrophotometric methods for simultaneous determination of acetaminophen and ascorbic acid in pharmaceutical formulation. Spectrochim. Acta A Mol. Biomol. Spectrosc. SPECTROCHIM ACTA A 266:120422. https://doi.org/10.1016/j.saa.2021.120422

Joseph XB, Sriram B, Wang S-F, Baby JN, Hsu Y-F, George M (2021) Revealing the effect of multidimensional ZnO@ CNTs/RGO composite for enhanced electrochemical detection of flufenamic acid. Microchem J 168:106448

Keeley GP, McEvoy N, Nolan H, Kumar S, Rezvani E, Holzinger M, Cosnier S, Duesberg GS (2012) Simultaneous electrochemical determination of dopamine and paracetamol based on thin pyrolytic carbon films. Anal. Methods 4:2048–2053. https://doi.org/10.1039/C2AY25156F

Keerthana P, Cherian AR, Sirimahachai U, Thadathil DA, Varghese A, Hegde G (2022) Detection of picric acid in industrial effluents using multifunctional green fluorescent B/N-carbon quantum dots. J Environ Chem Eng 10:107209

Lu D, Zhang Y, Wang L, Lin S, Wang C, Chen X (2012) Sensitive detection of acetaminophen based on Fe3O4 nanoparticles-coated poly (diallyldimethylammonium chloride)-functionalized graphene nanocomposite film. Talanta 88:181–186. https://doi.org/10.1016/j.talanta.2011.10.029

Ma B, Guo H, Wang M, Li L, Jia X, Chen H, Xue R, Yang W (2019) Electrocatalysis of Cu− MOF/graphene composite and its sensing application for electrochemical simultaneous determination of dopamine and paracetamol. Electroanalysis 31:1002–1008. https://doi.org/10.1002/elan.201800890

Madhu S, Manickam P, Pierre M, Bhansali S, Nagamony P, Chinnuswamy V (2018) Nanostructured SnO2 integrated conductive fabrics as binder-free electrode for neurotransmitter detection. Sens. Actuator A Phys 269:401–411. https://doi.org/10.1016/j.sna.2017.11.046

Montaseri H, Forbes PB (2018) Analytical techniques for the determination of acetaminophen: a review. Trends Analyt Chem 108:122–134. https://doi.org/10.1016/j.trac.2018.08.023

Nabatian E, Dolatabadi M, Ahmadzadeh S (2022) Application of experimental design methodology to optimize acetaminophen removal from aqueous environment by magnetic chitosan@ multiwalled carbon nanotube composite: isotherm, kinetic, and regeneration studies. Int J Environ Anal Chem 5:61–74

Nadafan M, Tohidifar MR (2020) Evaluation of structural, optical and dielectric properties of MWCNT-BaTiO3/silica ceramic nanocomposites. Ceram. Int 46:12243–12248. https://doi.org/10.1016/j.ceramint.2020.01.273

Najeeb J, Farwa U, Ishaque F, Munir H, Rahdar A, Nazar MF, Zafar MN (2022) Surfactant stabilized gold nanomaterials for environmental sensing applications–a review. Environ Res 208:112644

Pallavolu MR, Das HT, Kumar YA, Naushad M, Sambasivam S, Jung JH, Joo SW (2022) Marigold flower-like Sn3O4 nanostructures as efficient battery-type electrode material for high-performing asymmetric supercapacitors. J Electroanal Chem 920:116641

Pourmadadi M, Rajabzadeh-Khosroshahi M, Saeidi Tabar F, Ajalli N, Samadi A, Yazdani M, Yazdian F, Rahdar A, Díez-Pascual AM (2022) Two-dimensional graphitic carbon nitride (g-C3N4) nanosheets and their derivatives for diagnosis and detection applications. J. Funct. Biomater 13:204. https://doi.org/10.3390/jfb13040204

Pourmadadi M, Rahmani E, Rajabzadeh-Khosroshahi M, Samadi A, Behzadmehr R, Rahdar A, Ferreira LFR (2023) Properties and application of carbon quantum dots (CQDs) in biosensors for disease detection: a comprehensive review. J Drug Deliv Sci Technol 104156. https://doi.org/10.1016/j.jddst.2023.104156

Pourmadadi M, Yazdian F, Ghorbanian S, Shamsabadipour A, Khandel E, Rashedi H, Rahdar A, Díez-Pascual AM (2022) Construction of aptamer-based nanobiosensor for breast cancer biomarkers detection utilizing g-C3N4/magnetic nano-structure. Biosensors 12:921. https://doi.org/10.3390/bios12110921

Rajamani AR, Peter SC (2018) Novel nanostructured Pt/CeO2@ Cu2O carbon-based electrode to magnify the electrochemical detection of the neurotransmitter dopamine and analgesic paracetamol. ACS Appl. Nano Mater 1:5148–5157. https://doi.org/10.1021/acsanm.8b01217

Rizwan K, Rahdar A, Bilal M, Iqbal HM (2022) MXene-based electrochemical and biosensing platforms to detect toxic elements and pesticides pollutants from environmental matrices. Chemosphere 291:132820

Sharma V, Balaji R, Walia R, Krishnan V (2017) Au nanoparticle aggregates assembled on 3D mirror-like configuration using Canna generalis leaves for SERS applications. Colloids Interface Sci. Commun 18:9–12. https://doi.org/10.1016/j.colcom.2017.04.002

Sharma V, Balaji R, Kumar A, Kumari N, Krishnan V (2018) Bioinspired 3 D surface-enhanced Raman spectroscopy substrates for surface plasmon driven photoxidation reactions: role of catalyst and substrate in controlling the selectivity of product formation. ChemCatChem 10:975–979. https://doi.org/10.1002/cctc.201701616

Sivasankarapillai VS, Somakumar AK, Joseph J, Nikazar S, Rahdar A, Kyzas GZ (2020) Cancer theranostic applications of MXene nanomaterials: recent updates. Nano-Struct Nano-Objects 22:100457

Sriram B, Baby JN, Hsu Y-F, Wang S-F, George M (2021) Zirconium phosphate supported on g-C3N4 nanocomposite for sensitive detection of nitrite. J Electrochem Soc 168:087502

Tamilalagan E, Akilarasan M, Chen S-M, Chen T-W, Huang YC, Hao Q, Lei W (2020) A sonochemical assisted synthesis of hollow sphere structured tin (IV) oxide on graphene oxide sheets for the low-level detection of environmental pollutant mercury in biological samples and foodstuffs. Ultrason Sonochem 67:105164

Teng Y, Fan L, Dai Y, Zhong M, Lu X, Kan X (2015) Electrochemical sensor for paracetamol recognition and detection based on catalytic and imprinted composite film. Biosens. Bioelectron 71:137–142. https://doi.org/10.1016/j.bios.2015.04.037

Tkachenko OS, Souza LV, Deon M, Becker EM, de Menezes EW, Arenas LT, Benvenutti EV (2021) AgNP-decorated SBA-15 for MWCNT Paste modified electrode: a sensor for simultaneous voltammetric determination of paracetamol and sulfamethoxazole. Electroanalysis 33:29–37. https://doi.org/10.1002/elan.202060090

Vanova J, Malinak D, Andrys R, Kubat M, Mikysek T, Rousarova E, Musilek K, Rousar T, Cesla P (2022) Optimization of gradient reversed phase high performance liquid chromatography analysis of acetaminophen oxidation metabolites using linear and non-linear retention model. J Chromatogr A 1669:462956

Vinoth S, Wang S-F (2022) Detection of the neurodegenerative drug in a biological sample using three-dimensional sphere mixed metal oxide tailored with carbon fiber as an electrocatalyst by voltammetry technique. J Electrochem Soc 169:097511

Vinoth S, Wang S-F (2022) Modification of glassy carbon electrode with manganese cobalt oxide-cubic like structures incorporated graphitic carbon nitride sheets for the voltammetric determination of 2, 4, 6-trichlorophenol. Mikrochim. Acta 189:205. https://doi.org/10.1007/s00604-022-05305-6

Vinoth S, Govindasamy M, Wang S-F (2022) Solvothermal synthesis of silver tungstate integrated with carbon nitrides matrix composites for highly sensitive electrochemical nitrofuran derivative sensing in biological samples. Anal Chim Acta 1192:339355

Wan N, Lu X, Wang Y, Zhang W, Bai Y, Hu Y-S, Dai S (2016) Improved Li storage performance in SnO2 nanocrystals by a synergetic doping. Sci. Rep 6:1–11. https://doi.org/10.1038/srep18978

Wang K, Wu C, Wang F, Jing N, Jiang G (2019) Co/Co3O4 nanoparticles coupled with hollow nanoporous carbon polyhedrons for the enhanced electrochemical sensing of acetaminophen. ACS Sustain. Chem. Eng 7:18582–18592. https://doi.org/10.1021/acssuschemeng.9b04813

Wang J, Liu S, Luo J, Hou S, Song H, Niu Y, Zhang C (2020) Conductive metal-organic frameworks for amperometric sensing of paracetamol. Front Chem 8:594093

Wei M, Lu W, Liu G, Jiang Y, Liu X, Bai L, Cao X, Jia J, Wu H (2021) Ni2P nanosheets: a high catalytic activity platform for electrochemical detection of acetaminophen. Chin. J. Chem 39:1849–1854. https://doi.org/10.1002/cjoc.202100043

Yang L, Zhang B, Xu B, Zhao F, Zeng B (2021) Ionic liquid functionalized 3D graphene-carbon nanotubes-AuPd nanoparticles-molecularly imprinted copolymer based paracetamol electrochemical sensor: preparation, characterization and application. Talanta 224:121845

Yu S, Li H, Li G, Niu L, Liu W, Di X (2018) Reduced graphene oxide-supported gold dendrite for electrochemical sensing of acetaminophen. Talanta 184:244–250. https://doi.org/10.1016/j.talanta.2018.03.011

Zhang L, Hu Q, Chen G, Fang Y (2000) Simultaneous determination of the active ingredients in composite pseudoephedrine hydrochloride tablets by capillary electrophoresis. Anal. Chim. Acta 424:257–262. https://doi.org/10.1016/S0003-2670(00)01117-X

Zhang W, Liu S, Zhang Y, Ding X, Jiang B, Zhang Y (2019) An electrochemical sensor based on electro-polymerization of caffeic acid and Zn/Ni-ZIF-8–800 on glassy carbon electrode for the sensitive detection of acetaminophen. Biosens. Bioelectron 131:200–206. https://doi.org/10.1016/j.bios.2019.01.069

Zhang L, Si X, Yan X, He H, Deng D, Luo L (2020) A novel electrochemical sensor based on Au-rGO nanocomposite decorated with poly (L-cysteine) for determination of paracetamol. Curr. Anal. Chem 16:1063–1070. https://doi.org/10.2174/1573411016999200414145325

Zhao P, Ni M, Chen C, Zhou Z, Li X, Li C, Xie Y, Fei J (2019) Stimuli-enabled switch-like paracetamol electrochemical sensor based on thermosensitive polymer and MWCNTs-GQDs composite nanomaterial. Nanoscale 11:7394–7403. https://doi.org/10.1039/C8NR09434A